

Electronic Supplementary Material

A hydrogel-based antifouling solar evaporator for highly efficient water desalination

Xingyi Zhou,^{a,†} Fei Zhao,^{a,†} Youhong Guo,^{a,†} Yi Zhang,^b and Guihua Yu^{a,*}

* Correspondence to: ghyu@austin.utexas.edu.

† Contributed equally to this work

Contents

9

S1. Supplementary Methods

11 S1.1 Preparation of reduced graphene oxides (rGOs)

12 S1.2 Water transport measurements

13 S1.3 Water collection based on the CTH

14 S1.4 COMSOL Simulation

15 S1.5 Discussion of energy confinement

16

S2. Supplementary Figures

18 S2.1 The swelling ratio of the wall structure in the CTH.

19 S2.2 Chemical composition of the CTH.

20 S2.3 The carbon/oxygen ratio of different rGOs.

21 S2.4 Water absorbing experiment.

22 S2.5 Facilitated water transport in CTHs by capillary channels

23 S2.6 Evaluation of light absorption of CTHs.

24 S2.7 Optimization of PVA/water ratio.

25 S2.8 Optimization of rGO/PVA ratio.

26 S2.9 Water evaporation rate of CTHs with different areas.

27 S2.10 Water collection rate in closed system.

28 S2.11 Equivalent evaporation enthalpy of water in CTHs.

29 S2.12 One sun vapor generation performance of CTHs.

30 S2.13 COMSOL simulation of water transport in the CTH.

31 S2.14 Evaluation of purified simulating seawater based on the CTH.

32 S2.15 Crystalline antifouling of the CTH.

33 S2.16 Performance and crystalline antifouling of the CTH in high salinity water

34

S3. Supplementary References

1 **S1. Supplementary Methods**

2

3 **S1.1 Preparation of reduced graphene oxides (rGOs)**

4 For the preparation of reduced graphene oxide with various C/O ratios, different processing
5 methods were used. The graphite flakes bought from Sigma-Aldrich were directly dispersed in the
6 polyvinyl alcohol (PVA) solution to obtain CTH1 (Hydrogel with Capillary facilitated water
7 Transport). For CTH2, the reduced graphene oxide (rGO) was first made by hummers method
8 from graphite power,¹ then reduced by thermal reduction and dispersed in the PVA solution before
9 gelation. For CTH3, the rGO was first made by hummers method from graphite flakes,² followed
10 by gelation and then reduced by hydrazine. For CTH4, the rGO was first made by improved
11 hummers method from graphite flakes,³ followed by gelation and then reduced by hydrazine.

12 **S1.2 Water transport measurements**

13 The completely dried samples of CTHs with a weight of ca. 100 mg were immersed in 10 mL DI
14 water with a temperature of 40 °C. The weight of these samples was carefully tracked during the
15 swollen process until they were fully hydrated (no weight change in 30 min). Note that the weight
16 here was measured from CTHs which were wiped by a bibulous paper to remove the water in the
17 capillary channels. The recorded data from half-hydrated to fully-hydrated was used to evaluate
18 the water transport in CTHs.

19 **S1.3 Water collection based on the CTH**

20 For the water collection based on solar vapor generation, the area of the CTH is 1 cm² and the
21 temperature is ~25 °C. The purified water was directly collected from the transparent condenser
22 to avoid secondary contamination. DI water was added to the seawater every four hours to keep

1 the salinity constant during the collection. For each brine sample, 10 mL of the purified water was
2 collected for ICP test or the conductivity test.

3 **S1.4 COMSOL Simulation**

4 *SI.4.1 COMSOL Simulation of temperature distribution in CTHs*

5 Considering the water confinement of polymeric networks and the capillary channels, the heat
6 transfer in the CTH could be described by the equation given below:

$$7 \quad E_{in} = \rho C_p \frac{\partial T(x,t)}{\partial t} + \rho C_p v \cdot \nabla T(x,t) + \nabla [k \nabla T(x,t)]$$

8 Where the x and t are the space vector and time, respectively; ρ , C_p , and $T(x, t)$ are the mass
9 density, liquid thermal capacity and the local temperature, respectively; v and k are the fluid flow
10 speed and thermal conductivity of the aqueous medium; and E_{in} represents the thermal energy
11 input from the optical-thermal conversion. Along with the previous report, the heat transfer model
12 can be simplified as a semi-infinite medium for the Cartesian coordinate system.⁴ The numerical
13 simulations are conducted by COMSOL Multiphysics 4.4, under the steady and transient analysis
14 mode. Wherein, a constant heat flux of 0.1 kW m^{-2} occurs on the top ($Z = 500$), corresponding to
15 the solar energy input on the surface of the CTH (the evaporation consumed the energy of ca 0.9
16 kW m^{-2}). The 2D model is discretized into 1,000 elements. The convection heat transfer in the
17 polymeric network was disabled to describe the water restriction effect. To carry out a qualitative
18 analysis, it is assumed that the temperature of environment and water was set to $20 \text{ }^\circ\text{C}$ (293 K); the
19 balanced heat flux was 0.1 kW m^{-2} .

20

21 *SI.4.2 COMSOL Simulation of water transport in CTHs*

22 A steady model for water transport based on the biphasic mixture theory is derived in the CTH.
23 This combines the flow of fluid through a porous medium with different porosities and ignores the
24 complexity caused by deformation. The network of the polymer and the penetrating fluid in the
25 hydrogel will be taken as the penetrable solid and fluid, respectively.⁵ In the hydrogel, we consider
26 conservation of mass for the water phase of the fully swollen hydrogel as:

$$27 \quad \nabla \cdot v_p = \nabla \cdot [\phi_w \cdot (v_p - v_w)]$$

1 where ϕ_w is the water volume fraction, v_p and v_w are the intrinsic velocity of polymer and water
2 phases, respectively. Meanwhile, the conservation of momentum for the polymer and fluid phase
3 are given, respectively, by:

$$4 \quad \nabla \cdot \sigma_p + f_{pw}(v_w - v_p) = 0$$

$$5 \quad \phi_w \nabla \cdot P + \sum f_{iw}(v_w - v_i) = 0$$

6 Where σ_p , and f are the stress tensor and drag force between the two phases; and P represents the
7 intrinsic fluid pressure, comprising the osmotic pressure and the remaining part of the intrinsic
8 fluid pressure. Along with the experimental data, the predetermined v_{w0} was set on the top
9 boundary of the polymeric skeleton. Numerical simulations are conducted by COMSOL
10 Multiphysics 4.4, under the steady analysis mode. The 2D model is discretized into 1,000 elements.
11 To carry out a qualitative analysis, we also assume that the $f_{wp} = 10^{12} \text{ N s m}^{-2}$ in the polymeric
12 network to simplify the calculation.⁵

13

14 **S1.5 Discussion of Energy confinement**

15 Theoretically, the energy requirement for heating water can be calculated by

$$16 \quad Q = mC\Delta T$$

17 where Q is the heat energy needed, m is the mass, C is the specific heat ($4184 \text{ J kg}^{-1} \text{ }^\circ\text{C}^{-1}$ for water)
18 and ΔT is the temperature change, while the power input of 1 sun solar radiation is 100 mW cm^{-2} .
19 Therefore, the total energy input of our water system in 1 hour should be 360 J. It can achieve a
20 temperature change of $28.7 \text{ }^\circ\text{C}$ of 3 mL water, which is the amount of bulk water, indicating that
21 a light absorber with area of 1 cm^2 has the capability to heat 3 ml water if there is no energy
22 confinement effect.

23

24 Experimentally, the results have demonstrated that the main part (near 95%) of energy was used
25 to power the water vaporization near the evaporation surface, indicating that most of energy was

1 absorbed by the water vapor before dissipation. Since the core concept of the design is to confine
2 energy to the evaporation surface to power the water vaporization rather than heat water, it should
3 be rational to term such design as energy confinement.

4

5 Furthermore, as the temperature of evaporation surface is higher than the bulk water and ambient,
6 the temperature gradient will lead an inevitable energy dissipation to bulk water as well as
7 environment. The absolute energy confinement without any energy loss is actually unprocurable.
8 Nevertheless, the “energy confinement” can sufficient deliver the essential of material or structural
9 designs for advanced solar evaporators.

10

11

12

13

14

15

1 S2. Supplementary Figures

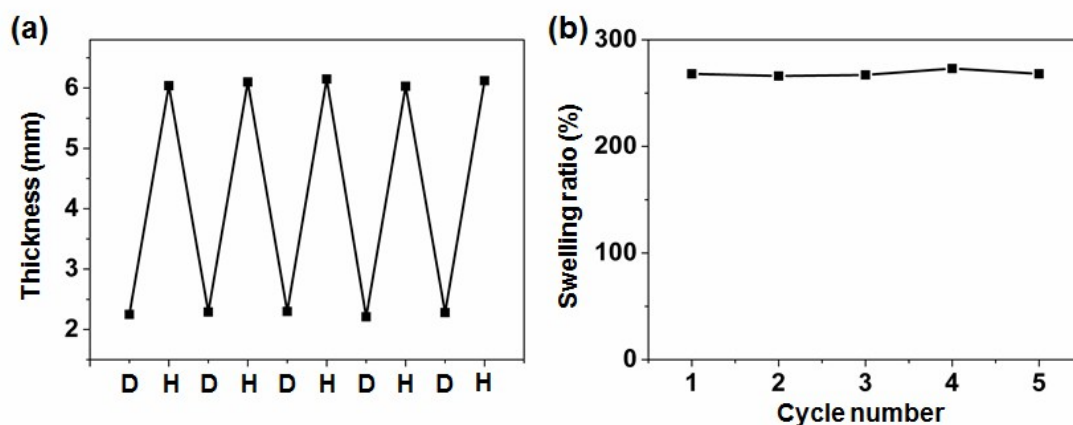
2

3 S2.1 The swelling ratio of the wall structure in the CTH.

4 To estimate the swollen behavior of the wall structure in the CTH, the repeatable shrinking-

5 swelling process of the CTH enabled a thickness change between ca. 2.3 mm to ca. 6.1 mm (Figure

6 S1a). The calculated swelling ratio along the dimension of thickness was ca. 270 % (Figure S1b).



7

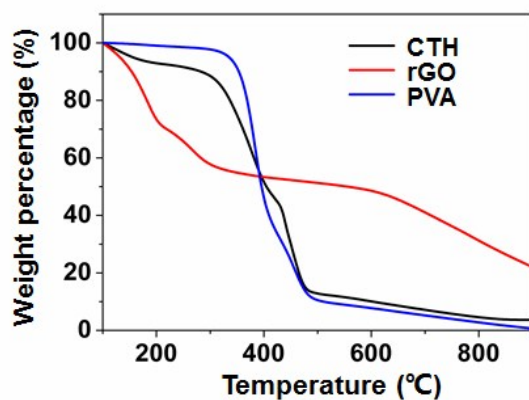
8 **Figure S1.** (a) The thickness of dried (D) and hydrated (H) state of the CTH. (b) Calculated

9 swelling ratio upon the dimension of thickness.

10

1 S2.2 Chemical composition of the CTH.

2 Figure S2 shows the TGA patterns of PVA gel, rGO and the CTH3 after pre-drying under 100 °C
3 for 5 h. With temperature changing from 100 to 900 °C, the weight loss starts from 350 °C to 480
4 °C for the PVA sample, while 100 °C to 900 °C for rGO sample, corresponding to the
5 disintegration of PVA polymer chains and rGOs. Therefore, the weight loss of the CTH could be
6 attributed to rapid decomposition of PVA (from 350 °C to 480 °C) and gradually decomposed rGO
7 (from 100 °C to 900 °C).



8

9

Figure S2. The TGA of as-prepared PVA aerogel, rGO and the dried CTH3.

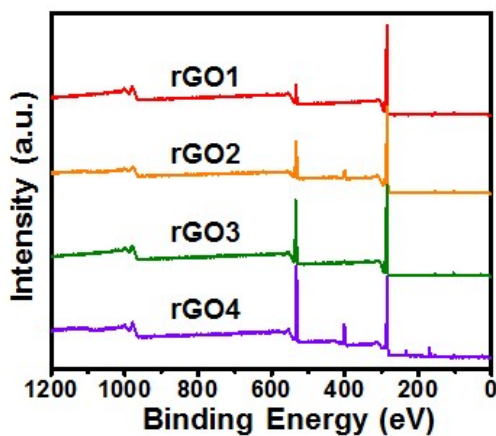
10

11

1 **S2.3 The carbon/oxygen ratio of different rGOs.**

2

3 The chemical composition of rGOs was analyzed by the X-ray photoelectron spectroscopy (XPS),
4 and the rGOs in CTH1 to CTH4 were labelled as rGO1, rGO2, rGO3 and rGO4. Figure S3 shows
5 the XPS spectra survey of these samples. The peaks located at 531 and 284 eV can be attributed
6 to the oxygen (O) and carbon (C) related bones.⁶ The element analysis of rGO1 to rGO4 revealed
7 an atomic C/O ratio of 132.3, 19.6, 12.7 and 4.9, respectively. From rGO1 to rGO4, the C/O ratio
8 gradually decreased, indicating the enhanced hydrophilicity.⁷



9

10

Figure S3. XPS of four rGOs evidencing the varying C/O ratio.

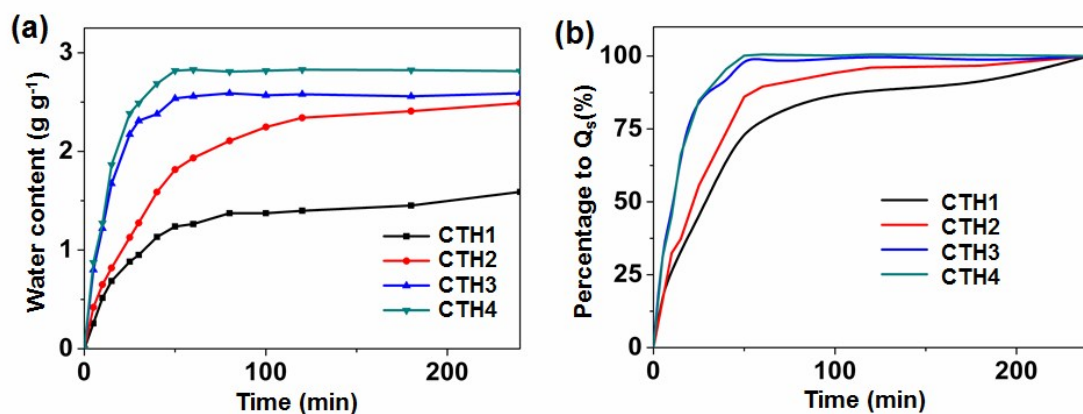
11

12

1 S2.4 Water absorbing experiment.

2

3 The water transport in polymeric gels can be represented by their swollen behavior. The water
4 transport in capillary channels was fast, while the water diffusion to molecular meshes depended
5 on the osmosis effect which was slower. Thus, the swelling of the polymeric network (i.e. water
6 transport to the molecular meshes) dominated the water absorbing rate. In this context, the swollen
7 behavior of hydrogels from CTH1 to CTH4 was investigated to evaluate the water transport. Note
8 that the water content (Q value) was measured from CTHs which were wiped by bibulous paper.
9 Owing to the strong capillary of bibulous paper, most of the water in capillary channels was
10 removed. As shown in Figure S4a, the dynamic analysis of swelling process was carried out to
11 evaluate the water transport in CTHs. And the Figure S4b which shows the corresponding
12 percentage to saturated water content (Q_s) over time was used to calculate the half-swollen time
13 from half-hydrated to fully-hydrated state.



14

15 **Figure S4.** (a) Water content (Q) variation and (b) percentage to the corresponding saturated water
16 content (Q_s) over time of each CTH.

17

18

19

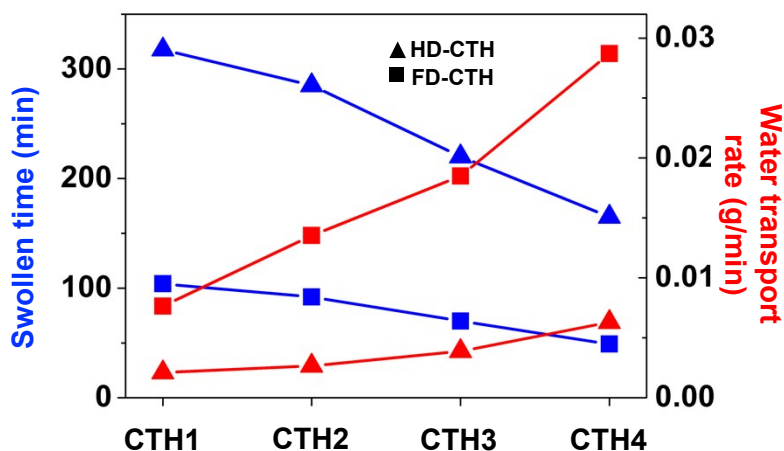
20

21

1 S2.5 Facilitated water transport in CTHs by capillary channels

2

3 Given that pores in hydrogels can be retained during dehydration process through freezing-drying
4 while baking will destroy microstructure of hydrogel forming dense xerogel,⁸⁻⁹ the xerogels of
5 CTH from freezing-drying and heating treatment (60 °C) were used to reveal the facilitation of
6 water transport enabled by capillary channels. Compared to CTH-xerogels with capillary channels
7 (i.e. freezing-dried CTH, FD-CTH), heating-dried CTHs (HD-CTH) presented longer half-swollen
8 time and slower water transport rate (Figure S5), and hence confirming that the capillary channels
9 in CTHs facilitate the internal water transport.



10

11 **Figure S5.** The swollen behavior of heating-dried CTHs (HD-CTH) and freeze-dried CTHs (FD-
12 CTH) from half-saturated to saturated state and calculated water transport rate

13

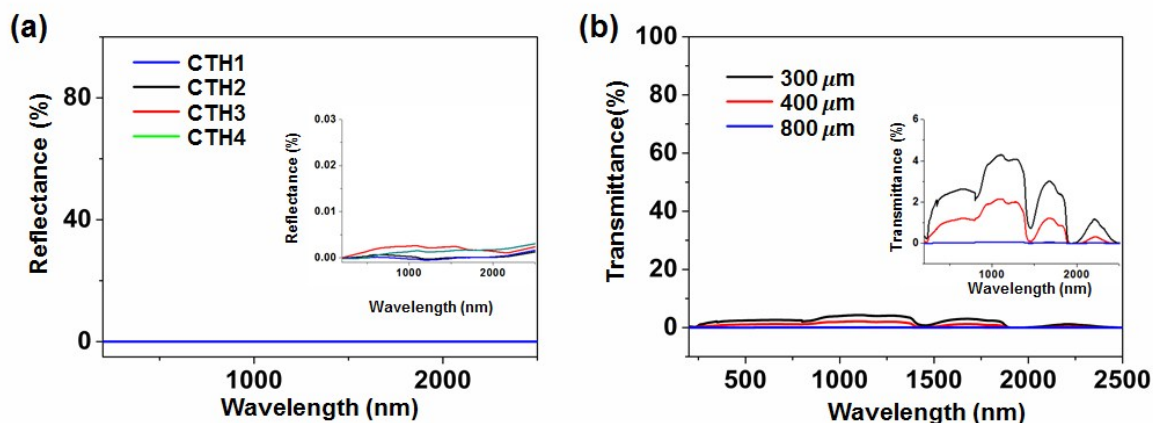
14

1 S2.6 Evaluation of light absorption of CTHs.

2

3 The reflectance and transparency of CTHs were studied by a UV–vis–NIR spectrophotometer. All
4 the CTH sheets (from CTH1 to CTH4) presented relatively lower reflectance (<1%) in a wide
5 wavelength range from 250 to 2500 nm (Figure S6a). The reflectance of CTHs is not sensitive to
6 the chemical composition. Additionally, since the transparency depended on the thickness of the
7 absorber, the transmittance of the CTHs with different thickness was carefully measured. For
8 comparison, we measured the transparency of CTH3 sheets with different thickness. The CTH
9 sheet with a thickness of 400 μm appears to be the optimum one for the full absorption of solar
10 illumination in a wide range of the spectrum (Figure S6b). Thus, the thickness of the effective
11 solar energy harvesting region in CTHs was around 400 μm . These results revealed a solar energy
12 harvesting efficiency over 98 % upon a CTH3 sheet.

13



14

15 **Figure S6.** (a) Reflectance and (b) transmittance spectra of CTHs in the wavelength range of 250–
16 2500 nm. Insets: High resolution curves of (a) reflectance and (b) transmittance.

17

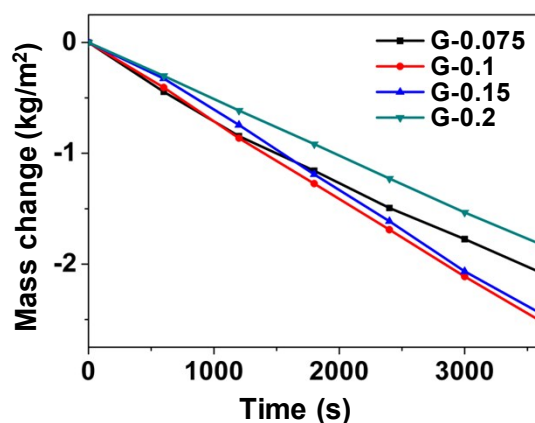
18

1 S2.7 Optimization of PVA/water ratio.

2

3 The weight ratio of polyvinyl alcohol/water (PVA/water) is 0.1:1 in CTHs. An optimized
4 PVA/water ratio can enable efficient water evaporation. As shown below, solar vapor generation
5 of the control samples with PVA/water weight ratio of 0.075:1, 0.1:1, 0.15:1 and 0.2:1, designating
6 as G-(Gels with PVA/water weight ratio of) 0.075, G-0.1, G-0.15 and G-0.2, respectively, were
7 tested under one sun. Since the rGO/PVA ratio of these control samples was 0.03:1, G-0.1 was the
8 CTH3 mentioned in the main text. The corresponding solar evaporation rates of G-0.075 to G-0.2
9 were ca. 2.35, ca. 2.50, ca. 2.44 and ca.1.82 kg m⁻² h⁻¹ (Figure S7). Thus, the PVA/water ratio of
10 0.1:1 in the CTH was proposed as an optimum value.

11



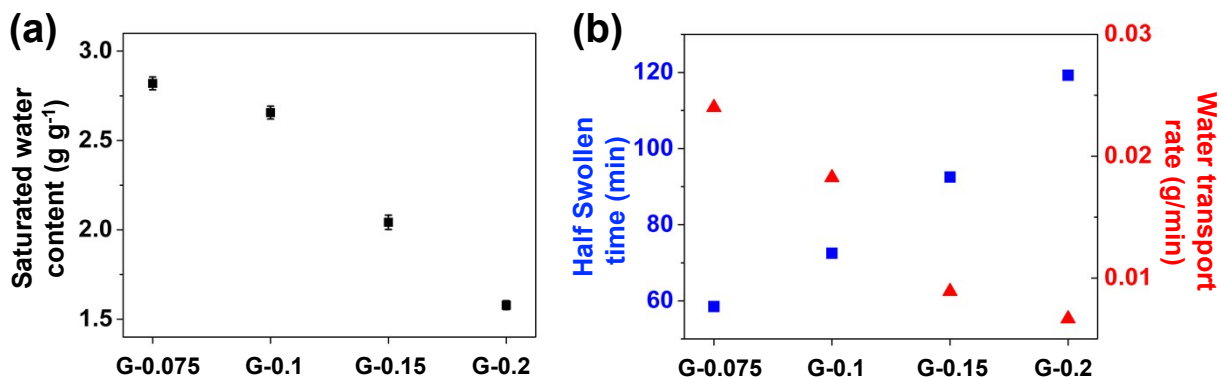
12

13 **Figure S7.** Mass change over time with G-0.075, G-0.1, G-0.15 and G-0.2 under one sun.

14 These CTHs exhibit different evaporation rates because water content and transport are influenced
15 by PVA/water ratio. To systematically assess the influence of PVA/water ratio on the water content
16 and transport in CTHs, G-0.075, G-0.1, G-0.15 and G-0.2 were investigated. The Q_s values from
17 G-0.075 to G-0.2 are 2.82, 2.66, 2.04 and 1.58 g per gram of the corresponding xerogel (i.e. g g-
18 1), respectively, indicating that the Q_s of the CTHs decreases as the polymer chains becomes

1 denser. (Figure S8a) In addition, the water transport in CTHs is evaluated by the dynamic analysis
2 of their swelling process. Upon one gram of xerogel, the G-0.075, G-0.1, G-0.15 and G-0.2 show
3 the V of 0.024, 0.018, 0.009 and 0.007 g min⁻¹, indicating slower water transport property of CTHs
4 with denser polymer networks (Figure S8b). G-0.075 exhibits relatively lower evaporation rate
5 compared with G-0.1 (CTH3 in the maintext) due to inadequate water transport, G-0.15 and G-0.2
6 also demonstrate relatively lower evaporation rate compared with G-0.1 due to high saturated
7 water content.

8



9

10 **Figure S8.** (a) The saturated water content and (b) The swollen behavior from half-saturated to
11 saturated state and calculated water transport rate in G-0.075, G-0.1, G-0.15 and G-0.2.

12

13

1 S2.8 Optimization of rGO/PVA ratio.

2

3 The weight ratio of reduced graphene oxide/polyvinyl alcohol (rGO/PVA) is 0.03:1 in CTHs (the
4 amount of rGO is considered to be same with the GO added into PVA solution before gelation).

5 An optimized rGO/PVA ratio can enable the accelerated solar vapor generation. As shown below,

6 solar vapor generation of the control samples with rGO/PVA weight ratio of 0.01:1, 0.03:1, 0.06:1

7 and 0.09:1, designating as GP-(gels with rGO/PVA weight ratio of) 0.01, GP-0.03, GP-0.06 and

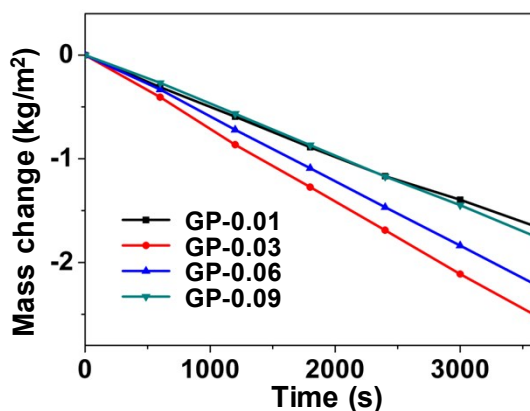
8 GP-0.09, respectively, were tested under one sun. Since the PVA/water ratio of these control

9 samples was 1:10, GP-0.03 was the CTH3 mentioned in the main text. The corresponding solar

10 evaporation rates of GP-0.01 to GP-0.09 were ca. 1.65, ca. 2.50, ca. 2.21 and ca. 1.75 kg m⁻² h⁻¹

11 (Figure S9). Thus, the rGO/PVA ratio of 0.03:1 in CTHs was proposed as an optimum value.

12



13

14 **Figure S9.** Mass change over time with GP-0.01, GP-0.03, GP-0.06 and GP-0.09 under one sun.

15

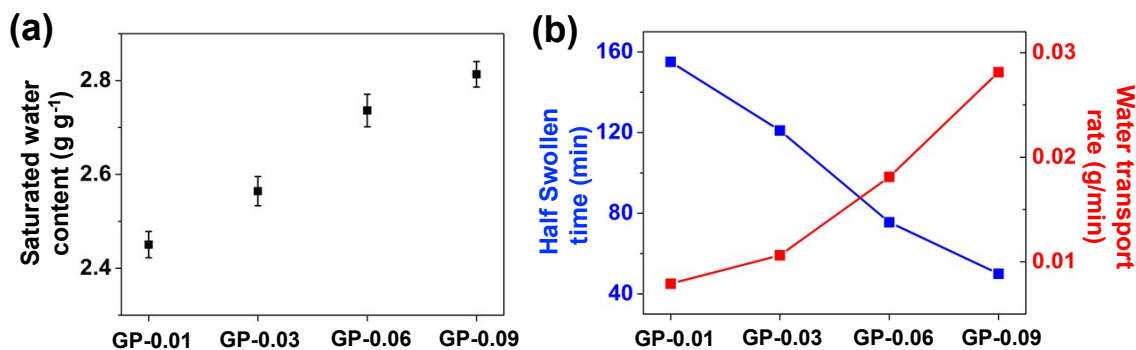
16 These CTHs present different evaporation rates because water content and transport are influenced

17 by rGO/PVA ratio. To systematically assess the influence of rGO/PVA ratio on the water content

18 and transport in CTHs, GP-0.01, GP-0.03, GP-0.06 and GP-0.09 were investigated. The Q_s values

19 from GP-0.01 to GP-0.09 are 2.45, 2.56, 2.74 and 2.81 g per gram of the corresponding xerogel

1 (i.e. g g^{-1}), respectively, indicating that the Q_s of the CTHs increases as the amount of rGO went
2 up (Figure S10a). In addition, the water transport in CTHs is evaluated by the dynamic analysis
3 of their swelling process. Upon one gram of xerogel, the GP-0.01, GP-0.03, GP-0.06 and GP-0.09
4 show the V of 0.008, 0.011, 0.018 and 0.028 g min^{-1} , indicating faster water transport property of
5 CTHs with higher rGO amount (Figure S10b). GP-0.01 exhibits relatively lower evaporation rate
6 compared with G-0.03 (CTH3 in the maintext) due to inadequate water transport and relatively
7 lower solar absorption, G-0.06 and G-0.09 also demonstrate relatively lower evaporation rate
8 compared with G-0.03 due to high saturated water content.



9

10 **Figure S10.** (a) The saturated water content and (b) The swollen behavior from half-saturated to
11 saturated state and calculated water transport rate in GP-0.01, GP-0.03, GP-0.06 and GP-0.09.

12

13

14

15

16

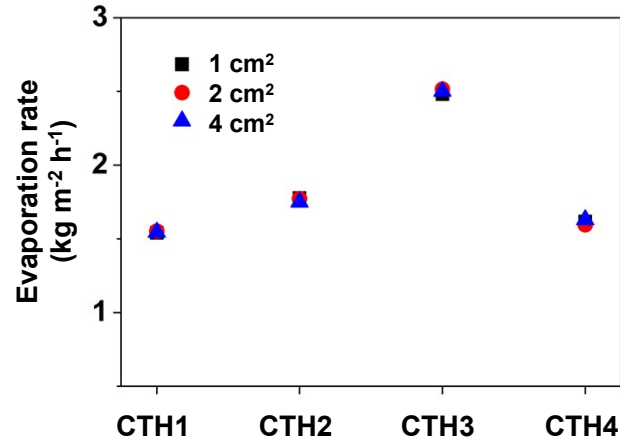
17

1 **S2.9 Water evaporation rate of CTHs with different areas.**

2 The evaporation rate of CTHs with area of 1, 2 and 4 cm² has been tested as shown Figure S11.

3 The results show identical normalized evaporation rates no matter the value comes from sample

4 with area of 1, 2 or 4 cm².



5

6 **Figure S11.** The water evaporation rate of different CTHs samples with area of 1, 2 and 4 cm²

7 under one sun (1 kW m⁻²)

8

9

10

11

12

13

14

15

1 **S2.10 Water collection rate in closed system.**

2

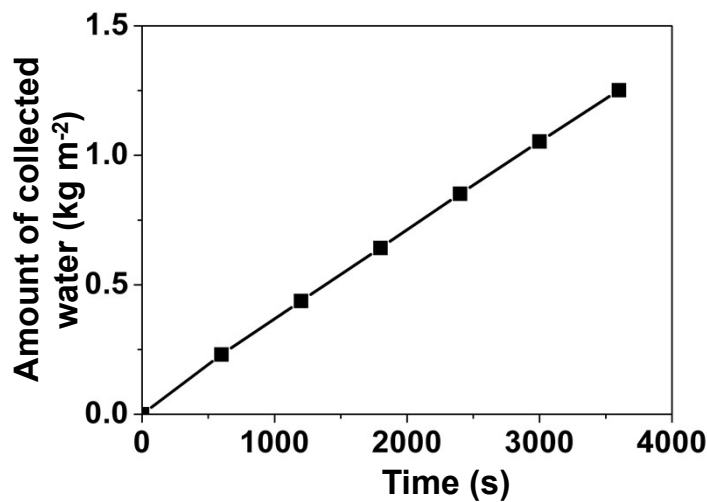
3 As a referable value to evaluate the practical potential of the CTH-based solar evaporator besides

4 water evaporation rate in open systems, the water collection rate obtained from water condensation

5 in closed systems was presented in Figure S12. In a closed collection system, the relative humidity

6 could reach the saturated value (100%) in a short period of time, which will depress the evaporation

7 of water. The purified water yield is $\sim 1.3 \text{ kg m}^{-2} \text{ h}^{-1}$.



8

9 **Figure S12.** Collected water amount over time under one sun (1 kW m^{-2})

10

11

12

13

1 **S2.11 Equivalent evaporation enthalpy of water in CTHs**

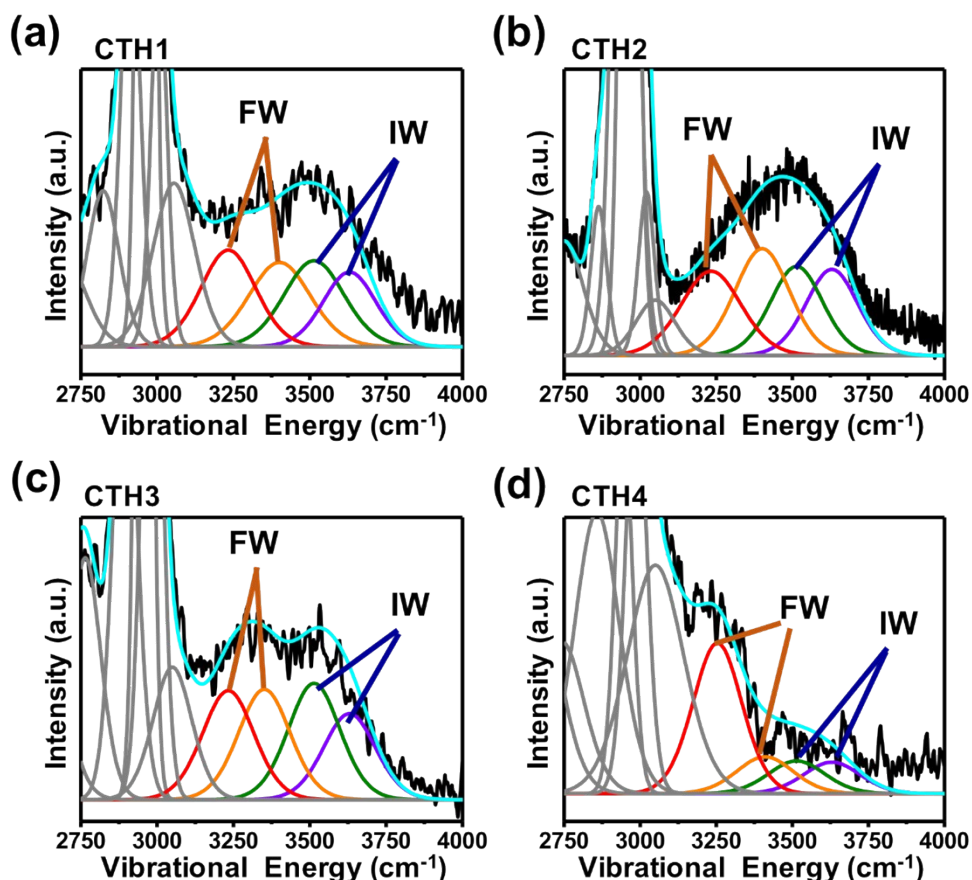
2

3 The water molecules in liquid phase have been demonstrated to be linked by hydrogen bonds,
4 forming water clusters.¹⁰ The systemic energy of these clusters can be minimized by their
5 configuration variation.¹¹ Additionally, such a configuration change only costs several fs in liquid
6 water.^{12, 13} As a result, every water molecule was confined to the dynamically stabilized cluster,
7 hence making the liquid water less evaporable. In line with such understanding, some preliminary
8 research reported the polymer derived configuration change of water clusters. For instance, due to
9 the strong hydrogen bonds between water molecules and –OH groups on PVA, most of these water
10 molecules form weak hydrogen bonds with the surrounding water molecules.¹⁴ The variation of
11 the molecular-level structure of water clusters was governed by the structure of the polymeric
12 network.¹⁴ Therefore, there are three kinds of water molecules in the polymeric network, which
13 can be categorized as free water (i.e. pure liquid water), intermediate water and bound water. It
14 has been demonstrated that the evaporation rate of intermediate water was ca. 86 times faster than
15 free water. Therefore, the water evaporation enthalpy can be reduced by the polymeric network
16 because of the existence of the intermediate water. And the amount of intermediate water can be
17 revealed by Raman spectra.¹⁵

18 As shown in Figure S13, the Raman spectra of water and four CTHs were fitted by four peaks
19 through the Gaussian function. The peaks observed at 3233, 3401, 3514, and 3630 cm^{-1} were
20 related to water.¹⁶ These peaks are classified as two types of modes: (1) Water molecules with four
21 hydrogen bonds, i.e., two protons and two lone electron pairs, are involved in hydrogen bonding
22 (the peaks at 3233 and 3401 cm^{-1}); (2) weak or non hydrogen-bonded water molecules in which
23 the hydrogen bonds of the water molecules have been broken partly or entirely (the peaks at 3514
24 and 3630 cm^{-1}). Within the band corresponding to the four hydrogen-bonded molecules, the peak
25 at 3233 cm^{-1} is associated with the collective in-phase vibrations of all molecules in the aggregate,
26 whereas the 3401 cm^{-1} peak is associated with vibration, which is not in-phase between the first
27 and higher shell of neighboring molecules (i.e., the out-of-phase mode of O-H stretching). The
28 peaks at 3514 and 3630 cm^{-1} correspond to the symmetric and asymmetric stretching of the weakly
29 hydrogen-bonded H_2O molecules, respectively.

30 The calculated molar ratio of intermediate water (IW), free water (FW) in, CTH1, 2,3 and 4 were
31 0.65:1, 0.83:1, 0.93:1, and 0.49:1, respectively. These results indicate that the CTHs contain more
32 intermediate water, hence facilitating the water evaporation. However, the intermediate water in

1 CTH4 is less compared with CTH1, 2 and 3, leading to slower evaporation rate as well as lower
2 efficiency.

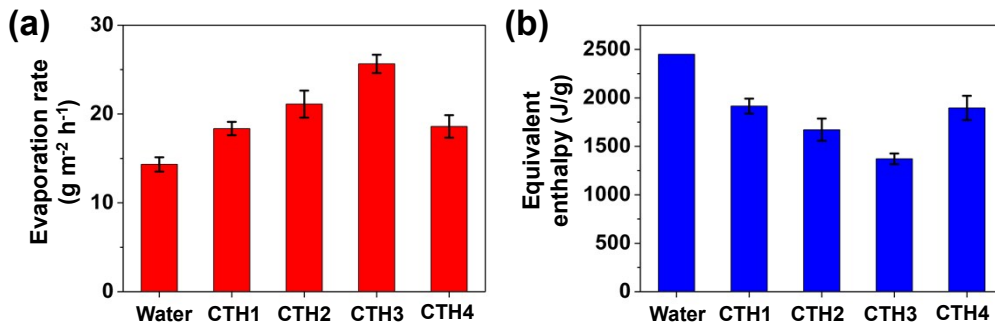


3
4 **Figure S13.** Fitting curves in the energy region of O-H stretching modes for (a) CTH1, (b) CTH2,
5 (c) CTH3 and (d) CTH4. The FW and IW represent free water and intermediate water, respectively.

6
7 The CTHs were almost fully hydrated during the solar evaporation, therefore the real vaporization
8 enthalpy, which only included the energy related to evaporation of free water and intermediate
9 water, should be even lower. A control experiment was designed to estimate the real vaporization
10 enthalpy as shown in Figure S14. The water and CTHs with the same superficial area were
11 synchronously set in a closed container together with the supersaturated potassium carbonate
12 solution (enabling stabilized RH of ca. 45%) under a temperature of ca. 25 °C and ambient air
13 pressure. The water evaporation rate and corresponding calculated E_{equ} were shown in Figure 14a
14 and S14b, respectively. The equivalent evaporation enthalpy (E_{equ}) of water in CTHs can be
15 estimated vaporizing the water with identical power input (U_{in}), which has

1 $U_{in} = E_0 m_0 = E_{equ} m_g$

2 where E_0 and m_0 were the evaporation enthalpy and mass change of bulk water; m_g was the mass
3 change of CTHs. The energy efficient was also calculated based on E_{equ} of corresponding CTHs.
4 The result demonstrates that different C/O ratio of rGO influence the vaporization enthalpy of
5 water. The introduction of rGO both chemically and structurally modifies the PVA-network in
6 CTHs. Therefore, the C/O ratio of rGO significantly influences the hydrophilicity of the polymeric
7 network, which has been demonstrated to dominate the latent heat decreasing



8

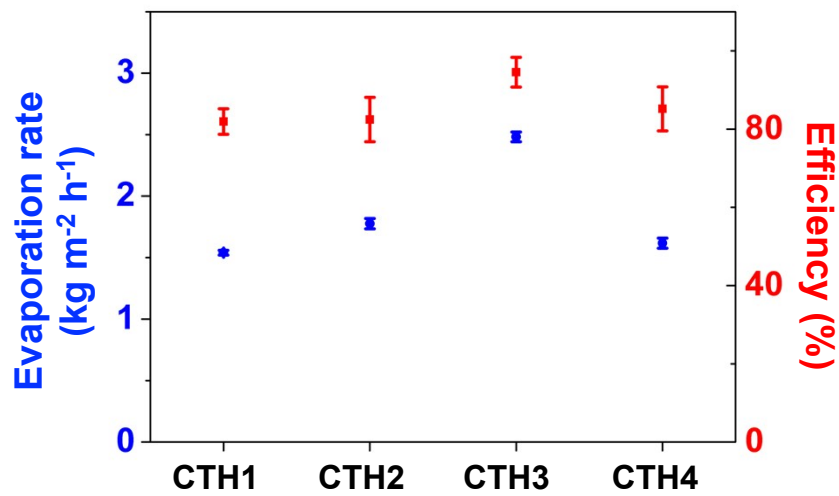
9 **Figure S14.** (a) Water evaporation rate in dark condition and (b) the calculated equivalent enthalpy
10 of water and CTHs.

11

12

1 **S2.12 One sun vapor generation performance of CTHs.**

2 Figure S15 shows the evaporation rate and corresponding efficiency of CTH1, 2, 3 and 4. The
3 result showed that the CTH3 provided the highest evaporation rate with a highly efficient energy
4 utilization. Compared with CTH3, CTH1 and CTH2 presented inefficient water transport which
5 seriously limited the evaporation rate as well as the utilization efficiency. Despite the fast water
6 transport in CTH4, the exorbitant water content will reduce the energy utilization efficiency,
7 leading to a lower evaporation rate.



8

9

10 **Figure S15.** One sun vapor generation performance of CTH1,2,3 and 4

11

12

1 **S2.13 COSML simulation of water transport in the CTH.**

2

3 A biphasic mixture model was used to simulate the water transport in the CTH (see *Supplementary*

4 *Methods* for details).¹⁵ The 2D mapping of water velocity distribution depicted a fast water

5 transport through the internal gaps against the surficial ($Z = 500$) water loss (Figure S16). Along

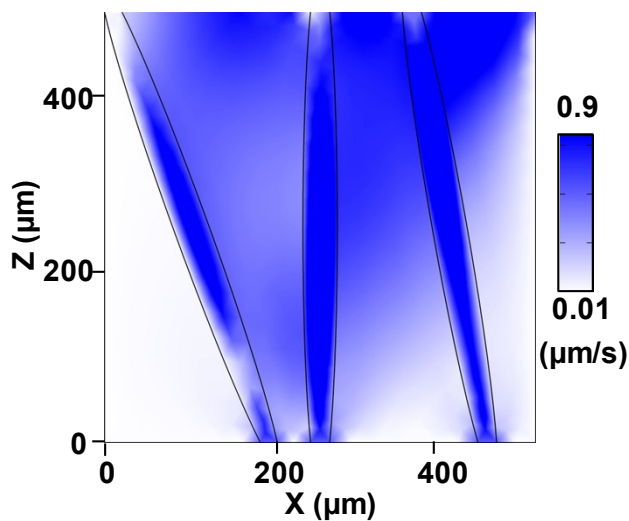
6 with our experimental data, the surficial water loss was estimated to be $0.69 \mu\text{m s}^{-1}$. The calculated

7 water transport from the bottom ($Z = 0$, corresponding to the interface of bulk water and the CTH)

8 to surface with a rate of $0.7 \mu\text{m s}^{-1}$ was supported by capillary channels. This fits well with the

9 experimental data, indicating the capillary facilitated water transport.

10



11

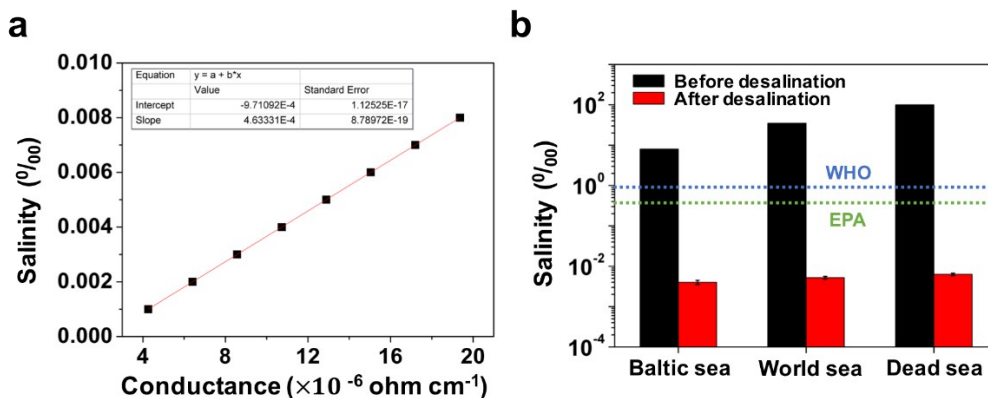
12 **Figure S16.** Theoretical simulation of water transport in the CTH by COMSL simulation.

13

14

1 S2.14 Evaluation of purified simulating seawater based on the CTH.

2 The salinity and conductance of the NaCl solution exhibited a linear dependency in a range of
3 salinity from 0.001 to 0.01 ‰. The standard curve was established for the calculation of salinity
4 of purified water from artificial seawater (Figure S17a). Three brine samples with representative
5 simulated salinities (g dissolved salt / kg seawater, i.e. ‰), Baltic sea (lowest salinity 8 ‰), world
6 sea (average salinity 35 ‰), and dead sea (highest salinity 100 ‰), were used and carefully tracked
7 by a conductivity test. As can be seen from Figure S17b., after desalination, the salinities of
8 artificial brine samples were all significantly decreased (about four orders of magnitude), which
9 are about two orders below drinking water standards defined by World Health Organization
10 (WHO, 1 ‰) and the US Environmental Protection Agency (EPA, 0.5 ‰).¹⁶



11

12 **Figure S17.** (a) Linear dependency of salinity and conductance of NaCl solution under 25 °C. (b)
13 The salinities of the three artificial seawater samples before and after desalination. The blue and
14 green dashed lines refer to the WHO and EPA salinity standards for drinkable water.

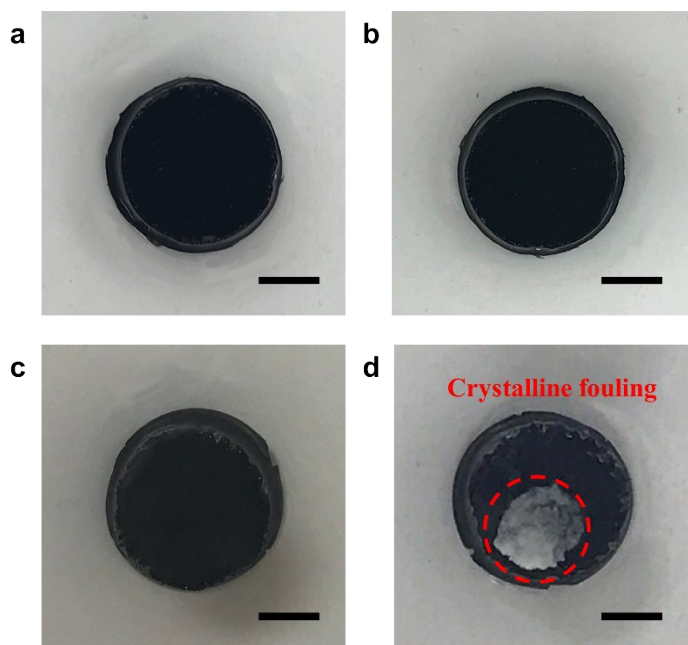
15

16

1 S2.15 Crystalline antifouling of the CTH.

2 The CTH (shown in Figure S18a) was used for solar vapor generation under one sun, after solar
3 irradiation for 96 h, salt crystals were not found at the surface of the CTH (as shown in Figure
4 S18b). Additionally, CTHs with different irradiation time (12 h, 24 h, 36 h, 48 h and 96 h) were
5 put to deionized water overnight, this process was repeated three times to ensure that all the salt
6 residuals in the hydrogel could be drifted to the deionized water for measurement. The washed
7 water was gathered and then carefully measured by the inductively coupled plasma spectroscopy
8 (ICP-OES). As shown in Figure 5c in the main text, the concentration of salt residual in the CTHs
9 is almost constant during a continuous solar desalination for 96 h, suggesting the restricted ion
10 accumulation, and hence realizes the crystalline antifouling functionality.

11 In addition, a rGO-based evaporator was prepared¹⁹ and used for solar desalination as shown in
12 Figure S18c. After 96 hours' irradiation under one sun, salt crystal appeared at the surface of the
13 evaporator (Figure S18d), indicating the crystalline fouling of the rGO-based evaporator.



14

15 **Figure S18.** Photographs of (a) the CTH evaporator before irradiation. (b) the CTH evaporator
16 after irradiation for 96h. (c) rGO-based evaporator before irradiation (d) rGO-based evaporator
17 after irradiation for 96h, showing the crystalline fouling due to the appearance of salt crystals at
18 the evaporation surface. Scale bar is 1cm

19

20

1 S2.16 Performance and crystalline antifouling of the CTH in high salinity water

2

3 In order to investigate the performance and crystalline antifouling of CTH in seawater with

4 different salinity. The evaporation rate of CTH3 in artificial seawater samples with salinity from

5 5 % to 25 % has been tested. As shown in Figure S19, the evaporation rate of CTH3 are almost

6 the same as long as the salinity of water is lower than 20 %. The evaporation rate slightly decreased

7 when the salt concentration was increased to 25 %. As shown in Figure S20, after exposure to salty

8 water (salinity =25%) for 1 h, the CTH was shrink, indicating a changing of micro-structure. Thus,

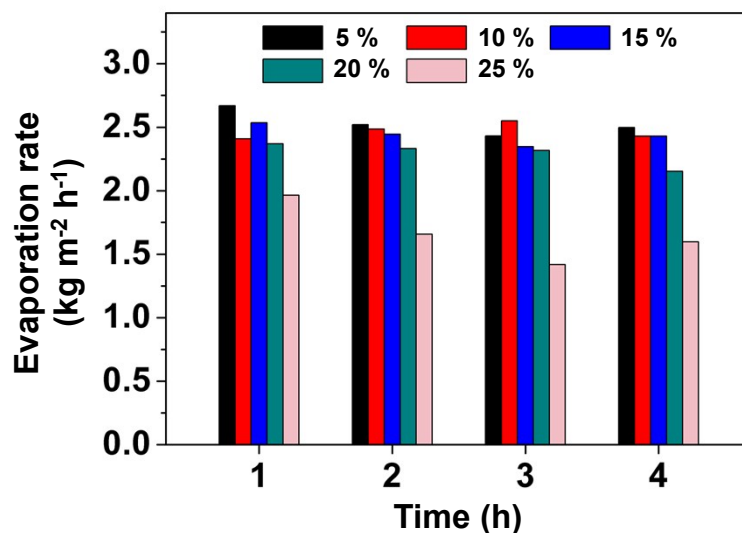
9 the decreased evaporation rate can be attributed to the partial dehydration of CTH caused by salt.

10

11 Regarding antifouling performance, there is no salt crystal could be found on the CTH after 12 h

12 continuous solar desalination of seawater with different salinity as shown in Figure S20. Such

13 result suggests that the antifouling performance could be retained in high salinity water.

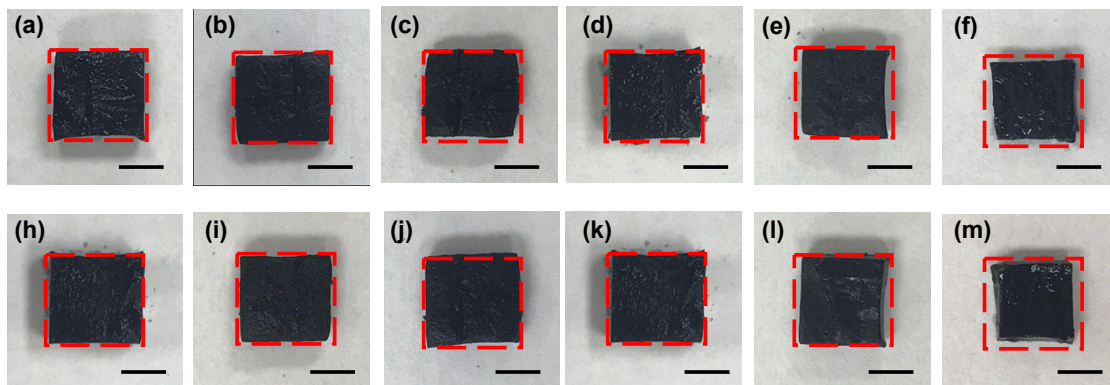


14

15 **Figure S19.** One sun vapor generation performance of CTH3 in simulated seawater with different

16 salinity from 5% to 25% (weight ratio).

17



1

2 **Figure S20.** Photographs of the CTH after exposure to salty water with salinity of (a) pure water
3 (b) 5 %, (c) 10 %, (d) 15 %, (e) 20 % and (f) 25 %. Photographs of the CTH after 12 h continuous
4 solar desalination of seawater with salinity of (g) pure water (h) 5 %, (i) 10 %, (j) 15 %, (k) 20 %
5 and (l) 25 %. Scale bar is 0.5 cm

6

7

1 S3. Supplementary References

- 2
- 3 1 W. S. Hummers Jr and R. E. Offeman, *J. Am. Chem. Soc.*, 1958, **80**, 1339.
- 4 2 J. Chen, F. Chi, L. Huang, M. Zhang, B. Yao, Y. Li, C. Li and G. Shi, *Carbon*, 2016, **110**,
- 5 34.
- 6 3 D. C. Marcano, D. V. Kosynkin, J. M. Berlin, A. Sinitskii, Z. Sun, A. Slesarev, L. B.
- 7 Alemany, W. Lu and J. M. Tour, 2010, **4**, 4806.
- 8 4 Y. Liu, S. Yu, R. Feng, A. Bernard, Y. Liu, Y. Zhang, H. Duan, W. Shang, P. Tao and C.
- 9 Song, *Adv. Mater.*, 2015, **27**, 2768.
- 10 5 X. Chen, Y. Jia, S. Sun, L. Feng and L. An, *Polymer*, 2009, **50**, 6186.
- 11 6 D. Yang, A. Velamakanni, G. Bozoklu, S. Park, M. Stoller, R. D. Piner, S. Stankovich, I.
- 12 Jung, D. A. Field and C. A. Ventrice, *Carbon*, 2009, **47**, 145.
- 13 7 S. Yang, W. Yue, D. Huang, C. Chen, H. Lin and X. Yang, *RSC Adv.*, 2012, **2**, 8827.
- 14 8 N. Annabi, J. W. Nichol, X. Zhong, C. Ji, S. Koshy, A. Khademhosseini, F. Dehghani,
- 15 *Tissue Eng Part B Rev.*, 2010, **16**, 371.
- 16 9 C. M. Hassan, N. A. Peppas, *J. Appl. Polym. Sci.* 2000, **76**, 2075.
- 17 10 M. Okumura, L. Yeh, J. Myers and Y. T. Lee, *J. Phys. Chem.*, 1990, **94**, 3416.
- 18 11 J.-C. Jiang, Y.-S. Wang, H.-C. Chang, S. H. Lin, Y. T. Lee, G. Niedner-Schatteburg and H.-
- 19 C. Chang, *J. Am. Chem. Soc.*, 2000, **122**, 1398.
- 20 12 M. Miyazaki, A. Fujii, T. Ebata and N. Mikami, *Science*, 2004, **304**, 1134.
- 21 13 M. V. Kirov, G. S. Fanourgakis and S. S. Xantheas, *Chem. Phys. Lett.*, 2008, **461**, 180.
- 22 14 Y. Sekine and T. Ikeda-Fukazawa, *J. Chem. Phys.*, 2009, **130**, 034501.
- 23 15 K. Kudo, J. Ishida, G. Syuu, Y. Sekine and T. Ikeda-Fukazawa, *J. Chem. Phys.*, 2014, **140**,
- 24 044909.
- 25 16 W. Monosmith, G. Walrafen, *J. Chem. Phys.*, 1984, **81**, 669.
- 26 17 E. Birgersson, H. Li and S. Wu, *J. Mech. Phys. Solids*, 2008, **56**, 444.
- 27 18 L. Zhou, Y. Tan, J. Wang, W. Xu, Y. Yuan, W. Cai, S. Zhu and J. Zhu, *Nat. Photonics*,
- 28 2016, **10**, 393.
- 29 19 Y. Xu, K. Sheng, C. Li and G. Shi, *ACS Nano*, 2010, **4**, 4324.